Phase-matching analysis of high-order harmonics generated by truncated Bessel beams in the sub-10-fs regime

C. Altucci,[1,2,*] R. Bruzzese,[1] C. de Lisio,[1] M. Nisoli,[3] E. Priori,[3] S. Stagira,[3] M. Pascolini,[4] L. Poletto,[4] P. Villoresi,[4] V. Tosa,[5,6] and K. Midorikawa[5]

[1]*Coherentia-INFM UdR di Napoli and Università "Federico II," Dipartimento di Scienze Fisiche—Complesso di Monte S. Angelo, via Cintia, 80126 Napoli, Italy*

[2]*Dipartimento di Chimica, Università della Basilicata, Potenza, Italy*

[3]*Ultras-INFM UdR di Milano, Dipartimento di Fisica, Politecnico di Milano, Milano, Italy*

[4]*Laboratory for Ultraviolet and X-ray Optical Research—INFM DEI—Università di Padova, Padova, Italy*

[5]*Laser Technology Laboratory, RIKEN, Japan*

[6]*National Institute for R&D in Isotopic and Molecular Technology, Cluj-Napoca, Romania*

(Received 2 December 2002; revised manuscript received 2 May 2003; published 19 September 2003)

We describe a very simple physical model that allows the analysis of high-order harmonic generation in gases when the pumping laser beam has an intensity profile that is not Gaussian but truncated Bessel. This is the typical experimental condition when sub-10-fs pump-laser pulses, generated by the hollow fiber compression technique, are used. This model is based on the analysis of the phase-matching conditions for the harmonic generation process revisited in view of the new spatial mode of the fundamental beam. In particular, the role of the atomic dipole phase and the geometric phase terms are evidenced both for harmonics generated in the plateau and in the cutoff spectral regions. The influence of dispersion introduced by free electrons produced by laser ionization has also been discussed in some detail. Spatial patterns of far-field harmonics are then obtained by means of a simplified algorithm which allows one to avoid the numerical integration of the harmonic beam propagation equation. Experimental spatial distributions and divergence angles of high-order harmonics generated in Ne with 7-fs titanium-sapphire pulses are compared with numerical simulations in various experimental conditions. The agreement between measurements and calculated results is found to be very satisfactory.

DOI: 10.1103/PhysRevA.68.033806 PACS number(s): 32.80.−t, 42.65.Ky, 42.65.Re

I. INTRODUCTION

The process of high-order harmonic (HOH) generation by rare-gas atoms in intense laser fields has become a reliable way to produce high-brightness, tabletop size, coherent radiation in the vacuum ultraviolet and soft-x-ray ranges (see Ref. [1] for a recent review). The unique properties of the harmonic emission have opened the way to relevant and new applications in (i) atomic and molecular core-level [2–4], photoionization [5], and plasma [6] spectroscopy, (ii) x-ray fluorescence analysis [7], (iii) time-resolved solid-state physics of surface states [8] and of UV photoemission spectroscopy [9], (iv) nanostructured and microstructured material characterization, such as porous silicon [10], (v) XUV interferometry for the diagnostics of dense plasmas [6,11,12].

Most of the mentioned applications require a high number of harmonic photons and, often, ultrashort harmonic pulses. Such a demand has been recently satisfied thanks to the availability of laser sources delivering few-optical-cycle pulses. The use of sub-10-fs titanium-sapphire laser beams, beyond opening the exciting way for the generation of single attosecond XUV radiation bursts [13,14], has allowed one to achieve very high harmonic brightness [15,16], due to the relatively high conversion efficiency of the harmonic generation process with such short pulses, and to the rather low-harmonic divergence angle.

One of the most successful methods for compressing ultrashort laser pulses down to the few-optical-cycle regime is the so-called hollow fiber compression technique [17]. So far, the only laser sources in the few-optical-cycle regime used for HOH make use, indeed, of this technique [15,18]. An important feature of the hollow fiber compression technique is that it produces a laser beam with a non-Gaussian spatial mode. In fact, by proper mode matching [19], the Gaussian laser beam at the hollow fiber input is dominantly coupled into its fundamental hybrid mode. The profile of the output beam amplitude, as a function of the radial coordinate, is then a zeroth-order Bessel function of the first kind, J_0 truncated at its first zero which falls in correspondence of the hollow fiber inner radius [16]. Moreover, the hollow fiber preserves the polarization of the input radiation and the output beam is found to be, as expected, nearly diffraction limited [20]. It is, then, particularly interesting and timing extending HOH analysis in the few-cycle regime to pump beams with Bessel and truncated-Bessel (TB) spatial modes.

Most of the presently available models, developed for HOH in the few-cycle domain, make use of a Gaussian fundamental beam [21–24]. Other schemes consider different peculiar generation geometries, that can possibly maximize the generation efficiency by optimizing the phase matching between the generated harmonic and the pump fields, such as HOH generation in hollow fibers filled with the nonlinear gaseous medium [25,26], or in a static cell where the generation takes place in a self-guided laser filament [27].

In a very recent paper [16] the analysis of HOH in the

*FAX: +39081676346. Electronic address: altucci@na.infn.it

few-cycle regime was for the first time carried out in terms of TB-pumping beams. In particular, the measured far-field spatial profiles of HOHs generated in a neon jet were compared with the results of numerical simulations based on the nonadiabatic strong-field approximation (SFA) [22,24,28]. Only when a TB-pumping beam was considered, the numerical simulations were able to properly reproduce the sub-10-fs experimental findings. On the contrary, numerical predictions based on a Gaussian pumping beam were significantly at odds with important experimental features, such as the harmonic conversion efficiency and spatial profile produced when the laser beam is focused just on the gas jet, and the dependence of the harmonic divergence angle on the position z of the gas jet relative to the laser focus.

A first, qualitative, physical explanation of these findings was outlined in Ref. [16] and is based on the different behavior of the on-axis pump-beam intensity for Gaussian and TB beams. This different behavior would affect the intrinsic, harmonic dipole phase, which is proportional to the laser intensity through the ponderomotive energy gained by the single active electron in the laser field [28,29]. Hence, the best phase-matching conditions of harmonics for Gaussian and TB-pump beams would be substantially different and this would determine the new interesting features observed in Ref. [16].

With the aim of interpreting the new experimental features observed in HOH generation with TB ultrashort pumping beams, we discuss here a very simple and versatile numerical model. It essentially relies on a graphic representation of the harmonic mismatch vector [30] which is immediately connected to the definition of the harmonic coherence length, and leads to generalized phase-matching conditions for HOH. The basic idea is to evaluate the potential efficiency of each point of the laser-gas interaction region to produce a single, elementary contribution to the final harmonic field, which is able to add up constructively to the other contributions. One can, thus, obtain a two-dimensional (2D) map of the phase-matching conditions, extended to all the generation region. The map takes into account the intrinsic dipole phase and the geometric phase depending on the spatial mode of the pumping laser beam. The influence of dispersion introduced by neutral atoms and by free electrons produced by gas medium ionization has also been analyzed in the Appendix. This influence turns out to be negligible when dealing with extremely short laser pulses [31,32] and relatively low gas pressures. We show that in this way one can reconstruct the whole wave front of the harmonic field, thus obtaining the direction of emission of each elementary contribution to the qth-order harmonic field and the spatial profiles of the far-field harmonics and divergence angle.

Such a considerable amount of physical information is obtained by calculating the single atom response in each point, namely, the atomic nonlinear dipole moment. This procedure avoids the problem of solving the propagation equations of the fundamental and harmonic fields through the nonlinear gas medium, which is numerically heavy and time consuming. As discussed in the following, our approach only rests on the assumption of a laser beam which is substantially unperturbed when passing through the gas jet. This assumption is pretty well fulfilled in the case of HOH generation in low-density gases (tens of millibars) with sub-10-fs optical pulses that minimize gas ionization [31,32], as in the case of Ref. [16]. Our model is particularly versatile, simple, and rapid if compared to long, *ab initio* HOH numerical calculations, and has the great advantage of providing a much more direct physical evidence of the role played by different aspects involved in the HOH generation process. Moreover, our approach can be easily generalized to any pumping beam geometry, as very recently demonstrated for HOH in xenon in conditions where self-guided propagation of the pulse is observed [33].

By using this model we have been able to analyze and explain the new and somewhat surprising main features of recent experiments carried out with few-optical-cycle TB-pumping beams. We have, in particular, obtained a remarkably good quantitative agreement between numerical and experimental values of the harmonic divergence angles and of their dependence on the propagation coordinate z.

This paper is structured into six sections. After a brief review of the main characteristics of ultrashort TB beams (Sec. II), and of the typical experimental results obtained when producing HOH with TB beams in the few-optical-cycle regime (Sec. III), we discuss in Sec. IV the theoretical aspects of the model. In Sec. V our results are reported and compared to the experimental values. Finally, Sec. VI contains a brief discussion and the final conclusions.

II. TRUNCATED-BESSEL ULTRASHORT BEAMS

TB beams are the typical output pulses of an ultrashort laser source whose final compression stage is based on the hollow fiber compression technique. In this section we derive and briefly discuss the main features of a TB-sub-10-fs beam in its focal region, where the interaction with the gas medium takes place in a HOH generation experiments.

In the typical experimental setup used in Refs. [16,34], 25 fs/1 mJ pulses, produced by a Ti:sapphire laser system with chirped-pulse amplification, are coupled into an argon-filled capillary where they spectrally broaden. The output pulses are then compressed by chirped mirrors to a typical duration of 5–7 fs. By proper mode matching, the incident radiation can be dominantly coupled into the fundamental EH_{11} mode of the hollow fiber, and the corresponding intensity profile as a function of the radial coordinate r is given by $I(r) = I_0 J_0^2(2.405r/a)$ with $r \leqslant a$, where I_0 is the on-axis peak intensity, $a = 0.25$ mm is the capillary radius, and J_0 is the zeroth-order Bessel function of the first kind. Finally, the compressed, sub-10-fs pulses are focused onto the gas jet by a 250-mm-focal-length silver mirror.

We recall at this stage that Bessel-like beams, such as Bessel-Gauss beams, were already employed for generating low-order harmonics (see, e.g., Ref. [35], and papers therein quoted). However, it is worth stressing the difference in the transverse profile of the pumping laser beam of those experiments with respect to the present case. TB and Bessel-Gauss beams, in fact, greatly differ from one another, for instance, in the far-field region the latter exhibits annular structures whereas the former does not.

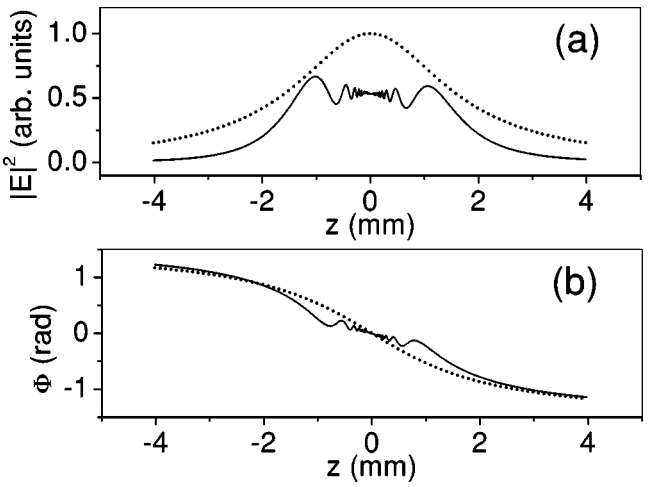

FIG. 1. On-axis features of the focused TB-beam: normalized beam intensity (a) and phase (b). The numerical results have been obtained by integrating Eq. (1) in the geometric configuration used in Ref. [16]. The dotted lines refer to the corresponding quantities for a Gaussian beam focused by the same optical system and with the same pulse energy.

According to the diffraction theory in the paraxial approximation, the transverse profile of the electric field associated to a TB beam, $E_{TB}(\zeta,r)$, at a distance ζ after a focusing mirror, can be expressed as [36]

$$E_{TB}(\zeta,r)=E_0\frac{-i}{\lambda_0 B(\zeta)}\exp\left[ik\left(\zeta+\frac{r^2}{2B(\zeta)}\right)\right]\int_0^a J_0\left(2.405\frac{\rho}{a}\right)\times J_0\left(-\frac{kr\rho}{B(\zeta)}\right)\exp\left[i\frac{A(\zeta)}{2B(\zeta)}\rho^2\right]\rho d\rho, \quad (1)$$

where $k=2\pi/\lambda_0$, and λ_0 is the central laser wavelength. Here, $A(\zeta)=1-\zeta/f$ and $B(\zeta)=d+\zeta(1-d/f)$ are the first two elements of the $ABCD$ matrix [37] of the optical system constituted by (1) the free space from the output of the hollow fiber to the focusing mirror for a distance $d \approx 2000$ mm, (2) the focusing mirror having focal length $f=250$ mm, (3) a further propagation after the mirror through the free space for a distance ζ. It is interesting to note that the condition $B=0$, fulfilled in the focal plane of the mirror, corresponds to $\zeta=\bar{\zeta}\approx 286$ mm, namely, ≈ 36 mm after the geometric focus of the mirror. At $\zeta=\bar{\zeta}$ the integrand in Eq. (1) becomes indeterminate. Nevertheless, the numerical integration of Eq. (1) can be carried out also in proximity of $\zeta=\bar{\zeta}$, as discussed in Ref. [38].

Some of the main TB-beam characteristics around the focusing plane have been plotted in Fig. 1, where the propagation coordinate ζ has been replaced by $z=\zeta-\bar{\zeta}$ for convenience. In parts (a) and (b) of Fig. 1, the normalized intensity $|E_{TB}|^2$ and the phase Φ_{TB} of the TB beam are, respectively, plotted as a function of z in the interaction region for $r=0$, i.e., on-axis. The same quantities for the same case of Gaussian beam, focused by the same optical system and with the same pulse energy, are also reported (dotted lines). The behavior of TB beams greatly differs from that of Gaussian beams: the beam intensity exhibits two peaks of nearly equal height at $z=1$ mm, with a region around $z=0$ characterized by quite high values of the beam intensity. In particular, the $z=0$ point is approached both from the left and the right side with a strongly damped oscillatory behavior. On the other hand, the on-axis phase of the TB beam is somewhat similar to that of a Gaussian beam, but for some small, damped, and chirped oscillations around $z=0$.

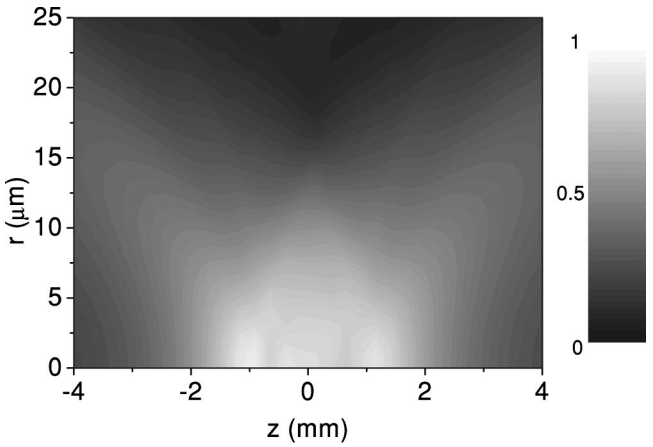

FIG. 2. Contour plot of normalized beam intensity extended to the interaction region. Brighter areas refer to higher-intensity values.

Finally, in Fig. 2 we show a contour plot of the TB beam normalized intensity relative to the interaction region (-4 mm$<z<4$ mm) extending 25 μm along the radial coordinate. White and black areas correspond to high- and low-intensity values, respectively. Once again the intensity map of a focused TB beam is very different from that of a Gaussian beam. In particular, in the area around $z=0$ the TB beam exhibits rather high-intensity values even off-axis at large r values (up to ≈ 10 μm). As a conclusion, we remark that for a focused TB beam a relatively large region around the focal plane ($z=0$) is characterized by a rather smooth and high intensity. This aspect will be crucial in the following interpretation of the experimental results.

III. HOH WITH SUB-10-FS TB BEAM

In this section we briefly recall the most important results achieved in recent HOH experiments by using sub-10-fs TB beams. The detailed description of the experimental apparatus and results can be found elsewhere [16,34].

A linearly polarized sub-10-fs Ti:sapphire laser pulse (typical pulse durations range from 5 to 7 fs) has been focused into a neon jet by a 250-mm-focal-length silver mirror. The laser-gas interaction length and local gas pressure have been estimated to be $\simeq 1$ mm and $\simeq 60$ mbars, respectively [39]. Harmonics, generated in the nonlinear interaction between the neon jet and the laser pulse, were dispersed and detected by means of a flat-field soft x-ray spectrometer and a high-resolution charge-coupled device (CCD) detector, the latter being constituted by a single-stage, intensified microchannel plate optically coupled to a low readout noise CCD camera. In this way, the spectrum and far-field pattern of the

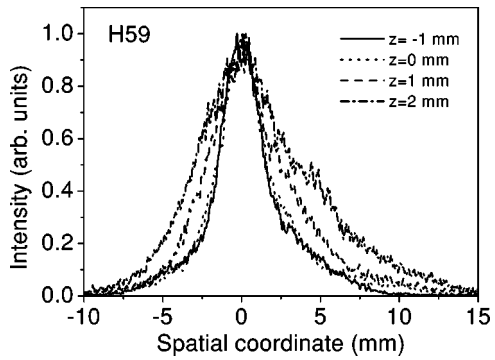

FIG. 3. Radial intensity profiles of H59 for various positions z of the gas jet with respect to the laser focus, recorded in the focal plane of the spectrometer.

harmonic beams have been simultaneously acquired.

The spatial properties of the harmonic radiation have been investigated as a function of the harmonic order and of the position z of the gas jet relative to the laser focus. Most of the measurements have been performed at a laser peak intensity at focus of $\simeq 9\times 10^{14}$ W cm^{-2}. Figure 3 shows the measured radial profiles of the 59th harmonic, recorded in the focal plane of the spectrometer for four different values of z, from $z=-1$ mm to $z=2$ mm. The harmonic angular distribution is strongly influenced by the gas jet position, the beam divergence continuously increasing with z. This feature is also confirmed by other harmonics in the plateau. An example is provided in Fig. 4 where the full width at half-maximum (FWHM) of the harmonic angular distribution is plotted versus z for H31, H49, and H55.

A second interesting feature of HOH generation with TB beams is that the divergence angle of harmonic radiation is observed to increase upon increasing the harmonic order in the plateau. On the contrary, a slight decrease of the harmonic divergence by increasing the order is observed in the cutoff (see Fig. 2 of Ref. [16]).

The above characteristics are substantially different from what was observed by using ordinary Gaussian pumping beams. In fact, models based on a Gaussian pump beam predict a rather poor spatial coherence for harmonics emitted at the focus and, in particular, a large divergence angle, whereas on-axis, collimated, and highly coherent harmonic

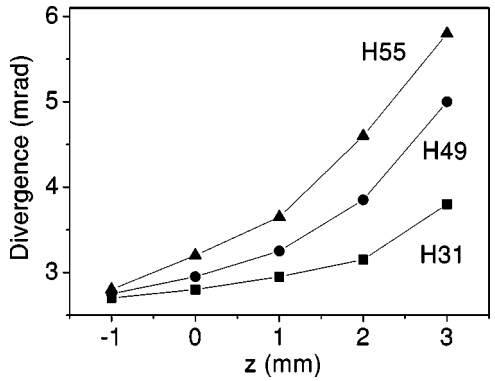

FIG. 4. Measured divergence (FWHM) of H31, H49, and H55 vs the position z of the gas jet relative to the laser focus [34].

emission is expected from a generating gas located a few millimeters *after* the laser focus, in the diverging pump beam [29]. These features have been largely confirmed in a number of experiments (see, for instance, Ref. [40] where the degree of spatial coherence of harmonics generated by a 60-fs Ti-:sapphire laser beam is experimentally characterized). On the contrary, the harmonics divergence angle measured in Ref. [16] is generally increasing with z, getting its maximum value just in the diverging beam, and keeping rather small values at the laser focus. As a consequence, also the harmonic brightness is low in the diverging beam, whereas it is found to be typically very high at focus.

IV. THEORETICAL ANALYSIS: THE COHERENCE MAP APPROACH

A. *Ab initio* calculations

The standard way to model HOH in the few-cycle domain consists in (i) calculating the single-atom response by using the nonadiabatic SFA and (ii) solving the coupled propagation equations of the fundamental and the harmonic beams, where the single-atom response is inserted as a source term (see, for instance, Refs. [22,24]). Briefly, by following the approach described in Ref. [24], the single-atom nonlinear dipole moment (in atomic units) is given by

$$d_{nl}(t)=2\mathrm{Re}\left\{ i\int_{-\infty}^{t} dt' d^*[p_{st}(t',t)-A(t')] \times d[p_{st}(t',t)-A(t)]E(t')\exp[-iS_{st}(t',t)] \times\left(\frac{\pi}{\epsilon+i(t-t')/2}\right)^{3/2}\right\}\exp\left[-\int_{-\infty}^{t} w(t')dt'\right], \quad (2)$$

where $E(t)$ is the electric field of the laser pulse, $A(t)$ is the associated vector potential, ϵ is a positive regularization constant, p_{st} and S_{st} are the stationary expressions of momentum and quasiclassical action of the active electron, respectively, d is the dipole matrix element for bound-free transitions. We stress here that, dealing with few-cycle laser pulses, the nonlinear dipole moment d_{nl} depends directly on the laser pulse electric field and its associated vector potential and not only on the laser pulse intensity $|E(t)|^2$. Medium ionization and ground state depletion are accounted for by using the Ammosov-Delone-Krainov (ADK) theory [41] and result in the last exponential scaling factor of Eq. (2), where $w(t)$ is the ADK tunnel ionization rate,

$$w(t)=\Omega_p|C_{n*}|^2\left(\frac{4\Omega_p}{\omega_t}\right)^{2n^*-1}\exp\left(-\frac{4\Omega_p}{3\omega_0}\right), \quad (3)$$

where

$$\Omega_p=\frac{I_p}{\hbar}, \quad \omega_t=\frac{e|E(t)|}{\sqrt{2m_eI_p}}, \quad n^*=Z\left(\frac{I_{ph}}{I_p}\right)^{1/2},$$

$$|C_{n*}|^2=\frac{2^{2n^*}}{n^*\Gamma(n^*+1)\Gamma(n^*)},$$

where Z is the net resulting charge of the ion ($Z=1$ in our case), ω_0 is the laser carrier angular frequency, I_p and I_{ph} are the ionization potential of the atomic species under use and of the hydrogen atom, respectively, e and m_e are the electron charge and mass, $\hbar$ is Planck's constant, and $\Gamma(x)$ is the Euler gamma function. The ionization rate in Eq. (3) can also be corrected at the highest laser peak intensities to account for atomic barrier suppression [42].

The near-field, fundamental and harmonic fields, after the nonlinear medium, are then worked out by integrating the Fourier transforms of the respective propagation equations in the paraxial approximation, written in a frame moving at the speed of light and therefore following the crest of the propagating fields (see, e.g., Eqs. (9) and (10) of Ref. [24]). The single-atom response becomes the source term for the propagation equation of the qth harmonic field E_q, via the nonlinear polarization field, $P_{nl}(r,z,t)=[n_0-n_e(r,z,t)]d_{nl}(r,z,t)$, n_0 being the neutral atomic density and

$$n_e(r,z,t)=n_0(r,z,t)\left\{1-\exp\left[-\int_{-\infty}^{t}w(t';r,z)dt'\right]\right\} \tag{4}$$

being the free-electron density in the gas.

By relying on this or similar models it has been possible to correctly simulate the results obtained in few-cycle, HOH experiments. In particular, the spatial characteristics of HOH measured in Ref. [16] can be well reproduced [16,34] by using a TB spatial pattern for the electric field. This way of reproducing and interpreting results of HOH experiments offers the advantage of being complete and rigorous, as it is based on an *ab initio* treatment of the problem, which takes into account all the potential physical factors that may affect the experimental observations. Nevertheless, it also implies two remarkable disadvantages: it is complicated and requires long computer time. Basically, complexity implies a hard interpretation of the measurements and of the physical mechanisms underlying the observed behaviors and a difficult characterization of specific physical parameters and of their role in the dynamics of HOH. The second disadvantage, concerning the long computation time taken by *ab initio*, HOH, numerical simulations becomes even more serious when dealing with fundamental beams with TB profiles. In fact, in this case, the amplitude and phase of the electric field exhibit fast oscillations around the nominal focus (see Fig. 1). As a consequence, solving the propagation equations of fundamental and harmonic fields becomes a hard task, because very small spatial integration steps are required both in the longitudinal and the radial direction. This also means that the final numerical predictions can be affected by a large overall uncertainty.

B. Coherence map analysis

We have thus followed a different route in order to interpret the results obtained in HOH experiments with TB beams. Our preliminary observation is that the fundamental field is substantially unperturbed while passing through the nonlinear medium in the experimental conditions of Ref. [16]. Among the possible sources of laser beam distortion, we can definitely neglect dispersion from neutral atoms and absorption at the laser wavelength ($\lambda_0=800$ nm) in our experimental conditions, as briefly discussed in the Appendix. Provided the remaining laser-induced ionization of the gaseous medium is small enough, the laser field mode is not significantly modified during the propagation through the interaction region. In order to check that this condition is fulfilled, we have calculated, by means of Eqs. (4) and (3), the free-electron density produced in the neon jet by a 7-fs, Ti:sapphire, TB beam focused as in Ref. [16] and thus reaching an on-axis peak intensity of 9×10^{14} W cm^{-2}. For this test a 1-mm, uniform neon medium has been assumed with a local pressure of $\simeq$60 mbars as in Ref. [16]. The result of such calculation shows that the overall (i.e., at $t\rightarrow\infty$) laser-induced, free-electron density $n_e(r,z)$ never exceeds $\simeq10\%$ of the neutral atoms. We have also checked that the components of the n_e spatial gradient ∇n_e are not too steep to perturb the phase behavior of the considered TB beam during the propagation. This point has been discussed, together with the problem of the influence of free-electron dispersion on HOH phase-matching conditions, in the Appendix. In particular, we have demonstrated that, in our experimental conditions, these effects do not significantly modify the harmonic phase-matching conditions and the far-field harmonic pattern.

We have also numerically estimated the influence of the propagation through the ionizing gas medium of the fundamental laser beam by calculating its output amplitude and phase (r,z) distributions. The final perturbation introduced by the gas medium, which is totally negligible for the field amplitude, is restricted to less than a few percent for the field phase value.

Moreover, we have assumed a power-law dependence of the atomic nonlinear dipole moment on laser intensity $d_{nl}\propto I^5(\boldsymbol{r},t)$, as widely found in literature (see, for example, Ref. [43]). In order to check the validity of such an assumption we have worked out the nonadiabatic SFA result for the nonlinear polarization field in neon at the 45th harmonic frequency, $P_{nl}(r,z,\omega=45\omega_0)=P_{45}(r,z)$, representative of harmonics in the plateau, by using Eq. (2) and the laser field spatial profile as calculated from Eq. (1). The temporal envelope of the laser intensity has been assumed Gaussian, lasting 7 fs at FWHM, and the laser peak intensity at focus has been again taken as 9×10^{14} W cm^{-2}. We have found that the result can be put in the form $P_{45}(r,z)\propto I(r,z)^{q'(r,z)}$ where the exponent $q'(r,z)$ is confined between 4.5 and 5 when moving the source point (r,z) all over the interaction region. Therefore, our simplification is largely justified. However, it is worth pointing out that the above assumptions are quite general and do not severely restrict the field of application of our analysis, since they apply each time the laser field is practically unperturbed while passing through the nonlinear medium. Moreover, this is what occurs up to rather high peak intensity when dealing with few-cycle pulses [44].

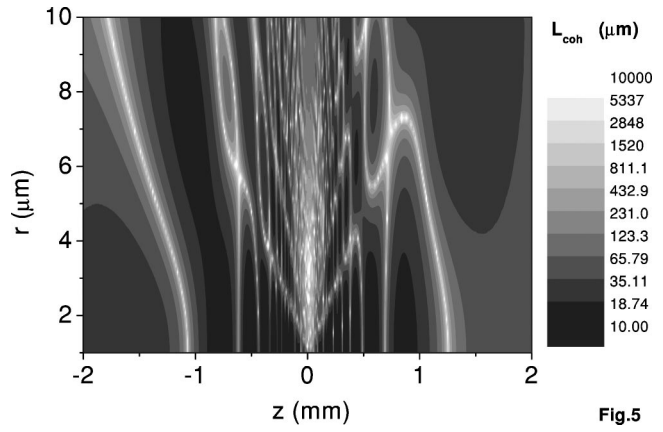

FIG. 5. Contour plot, extended to the interaction region, of the coherence length map L_{coh} for the 45th harmonic generated in ≈ 60 mbars of neon by a 7-fs, Ti:sapphire TB beam. The intensity at focus is $I(r=z=0)=7\times10^{14}$ W cm^{-2} and the beam diameter at $z=0$ is ≈ 15 μm (see Fig. 1).

We have, then, analyzed the spatial behavior of the harmonics' coherence length L_{coh} defined as [30]

$$L_{coh}=\frac{\pi}{\Delta k}, \tag{5}$$

where Δk is given by

$$\Delta k = k_q - |\boldsymbol{k}_{pol}| = \frac{2\pi n(\omega_q)}{\lambda_q} - |\boldsymbol{k}_{pol}|, \tag{6}$$

$n(\omega_q)$ being the nonlinear medium refractive index at the qth harmonic angular frequency, and $\lambda_q=\lambda_0/q$ being the qth harmonic central wavelength. Δk represents the norm of the space-dependent mismatch vector $\Delta\boldsymbol{k}(r,z)$, which is parallel to the polarization wave vector $\boldsymbol{k}_{pol}$. The wave vector $\boldsymbol{k}_{pol}$ at the point (r,z) reads [45]

$$\boldsymbol{k}_{pol}=\boldsymbol{\nabla}\left[q\frac{2\pi n(\omega_0)}{\lambda_0}z+q\Phi_{TB}(r,z)+\Phi_{dip}(r,z)\right], \tag{7}$$

Φ_{TB} being the phase of the focused TB beam and $\Phi_{dip}(r,z)=\alpha I(r,z)$ is the intensity-dependent atomic dipole phase [29] with $\alpha\approx -24.8\times10^{-14}$ cm^2/W for harmonics in the plateau [30]. We point out that Eqs. (5) and (7), in which dispersion is neglected, have been generalized in the Appendix to account for possible other mismatch contributions arising from dispersion from neutrals and from laser-induced free electrons.

C. Numerical results

We remark that all the simulations reported in this section have been performed for a uniform neon medium having a local pressure of ≈ 60 mbars in order to match the experimental conditions of Refs. [16,34].

Figure 5 also shows the principal feature of the coherence length pattern when using TB-pump beams. Contrary to what is obtained when using a laser pump beam with a Gaussian profile (see Refs. [30,45], for instance), the area of the interaction region characterized by favorable phase-matching conditions (high values of the coherence length) is now located around $z=0$, and not in the diverging laser beam ($z>0$ according to our sign convention). There are also other few spatial domains where good phase matching can be achieved, but they are very small, and generally located well off-axis, where the laser intensity is much lower.

The coherence map approach is thus able to provide a clear physical interpretation of why phase matching for HOH generated by TB beams is so different from the case of Gaussian pump beams: the zone of the nonlinear gas medium around $z=0$ is now favorite for the construction of a macroscopic HOH signal, in total agreement with experimental observations.

We have then tested the dependence of our results on the harmonic order. Figure 6 shows the coherence length map of four harmonics. The first, i.e., H25, lies in the initial part of the plateau [case (a)]; H45 (b) and H59 (c) in the middle, and H69 (d) at the end of the plateau. All cases have been calculated for the highest laser intensity ($\approx 9\times10^{14}$ W cm^{-2}). Since H25 and H45 exhibit very similar coherence length patterns, it is worth noticing that we have enlarged the region around $z=0$ in (a), in order to highlight the details of the most important region of the pattern. Apart from a quite flat central region of high average coherence length around $z=0$, there is a ring-type structure constituted by a series of many thin rings of good phase-matching accumulating towards the plane $z=0$. The central flat region, where the macroscopic harmonic signal grows up, originates from the decrease of the rapid oscillations of both TB electric-field amplitude and phase (see Fig. 1). Such a decrease implies a more stable behavior of the phase terms Φ_{dip} and Φ_{TB} in Eq. (7), and we will see in the following section how this condition also corresponds to minimizing the divergence angle of the emitted harmonics. The average coherence length is now reduced as compared to the values of Fig. 5, where the laser intensity was lower. For the common case of the 45th harmonic, average values of L_{coh}, evaluated in the regions where the harmonic field is effectively constructed, decrease from ~ 500 μm of Fig. 5 to ~ 100 μm of Fig. 6, due to the higher values reached by Φ_{dip} [see Eqs. (7) and (5)]. It is worth pointing out that peak values of L_{coh} are strongly diminished by the effect of the free-electron dispersion as demonstrated in the Appendix. Nevertheless, this effect is locally restricted to extremely small regions around the peaks of L_{coh}, whereas the overall contour plot of the average coherence length, extended to the interaction region, is almost unmodified even taking into account free-electron dispersion. Thus, the influence of free-electron dispersion on the general characteristics of the average harmonic coherence length is negligible, as analyzed in detail throughout the Appendix. Typical values of L_{coh} referred to the regions around $z=0$, where the largest part of the generated harmonic field is constructed, are in the range of some hundreds of microns, despite the presence of a small percentage ($\leqslant 10\%$) of laser-induced free electrons. This behavior is of general validity for all the investigated harmonics, in our experimental conditions. The values of L_{coh} values for the 25th and 45th

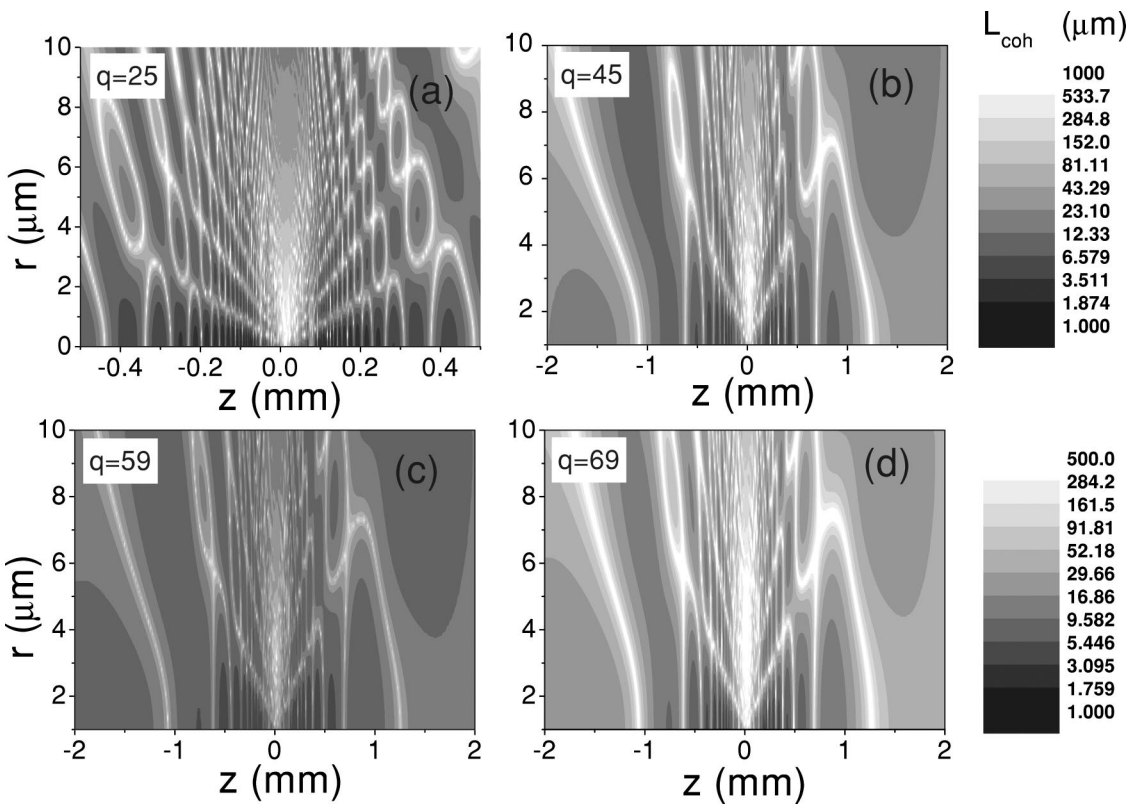

FIG. 6. Two-dimensional phase-matching maps of H25 (a), H45 (b), H59 (c), and H69 (d) obtained for a laser intensity of 9×10^{14} W cm^{-2}. The other parameters are the same as in Fig. 5. The coherence length L_{coh} is expressed in micrometers. Equal L_{coh}-value scales are used for H25 and H45 and for H59 and H69, respectively.

harmonic case are about the same. The 59th and 69th harmonics [Figs. 6(c) and 6(d), respectively] have, instead lower average coherence lengths, ranging in the typical case within 50–200 μm. The 69th harmonic has, anyway, values of L_{coh} higher than those of H59. The region of good phase matching is also wider for H69 than for H59, although it must be considered that, due to the higher laser intensity required, H69 is emitted in a smaller area of the nonlinear medium concentrated along the propagation axis.

In order to compare the behavior of the coherence length map for harmonics in the plateau and in the cutoff region, we have studied the same harmonic, namely H69, at two different laser intensities, $I=5\times10^{14}$ W cm^{-2} and $I=9\times10^{14}$ W cm^{-2}. At the lower intensity H69 lies in the cutoff, and the corresponding coherence length map is reported in Fig. 7(a). This has to be compared with Fig. 6(d) where, for $I=9\times10^{14}$ W cm^{-2}, the same harmonic lies in the plateau. Striking differences can be observed. When H69 lies in the cutoff, a considerably large region of very high L_{coh} values (typically larger than to 0.5 mm) is obtained for positive z values ($z\approx1.4$–1.8 mm). This is pretty similar to the best phase-matching conditions observed when using Gaussian pump beams, while it is very different from that obtained when the same harmonic lies in the plateau [Fig. 6(d)].

Our analytical approach clearly indicates that the different features observed in Fig. 7(a) are caused by the behavior of the harmonic field phase. This is shown in Fig. 7(b), where the on-axis, total harmonic field phase for H69 (solid curves) is plotted versus z, in the interval 1–2 mm, both in the cutoff $\Phi_{tot}^{(cutoff)}$ (top curve) and in the plateau case $\Phi_{tot}^{(plateau)}$ (bottom curve). In the same figure we have also reported the atomic dipole phase $\Phi_{dip}=\alpha I(r,z)$, in both cases (dashed lines), and, finally, the geometric phase of the TB 69th harmonic $\Phi_{69,TB}$ (dotted curve), which is obviously the same in the plateau and cutoff regions. At the lower intensity, when H69 belongs to the cutoff and for the only dominant electronic trajectory in this region [30] the coefficient α is given by $\alpha^{(cutoff)}=-13.7\times10^{-14}$ cm^2/W, and Φ_{dip} is basically a slowly increasing function of z. On the contrary $\Phi_{69,TB}$ slowly decreases with z. Since both phase contributions have comparable magnitudes (between 50 rad and 70 rad), the resulting total harmonic phase $\Phi_{tot}^{(cutoff)}$ of H69 shows a very flat overall behavior in the range 1 mm$\leqslant z\leqslant$2 mm. Similar features are also observed for other harmonic orders, and off-axis.

On the contrary, when H69 lies in the plateau [bottom curves of Fig. 7(b)], the atomic dipole phase is, in absolute value, almost four times bigger than in the cutoff, the laser peak intensity being about twice the value of the former case ($I\approx11\times10^{14}$ W cm^{-2} in the left high intensity lobe of the TB beam) and the coefficient $\alpha=\alpha^{(plateau)}=-24.8\times10^{-14}$ cm^2/W for the dominant electronic trajectories in the plateau [30]. Hence, $\Phi_{dip}^{(plateau)}$ strongly dominates the

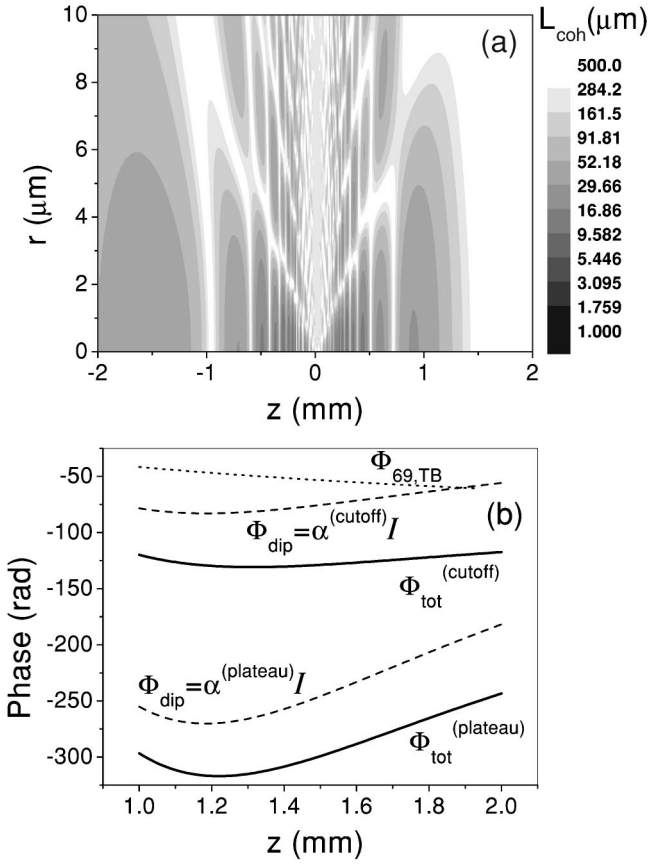

FIG. 7. (a) Coherence length map for H69 in neon for a laser intensity of 5×10^{14} W cm^{-2}. At this laser intensity the 69th harmonic belongs to the cutoff of the harmonic spectrum. (b) On-axis phases vs z for H69. The top curves refer to the geometric phase $\Phi_{69,TB}$ (dotted curve), to the atomic dipole phase for H69 in the cutoff, $\Phi_{dip}=\alpha^{(cutoff)}I$ (top dashed curve), and to the overall harmonic field phase $\Phi_{tot}^{(cutoff)}$ (top thick solid curve). The two bottom curves represent the atomic phase for H69 when it lies in the plateau (same laser peak intensity as Fig. 6) $\Phi_{dip}=\alpha^{(plateau)}I$ (bottom dashed curve) and the total harmonic field phase $\Phi_{tot}^{(plateau)}$ (bottom thick solid curve).

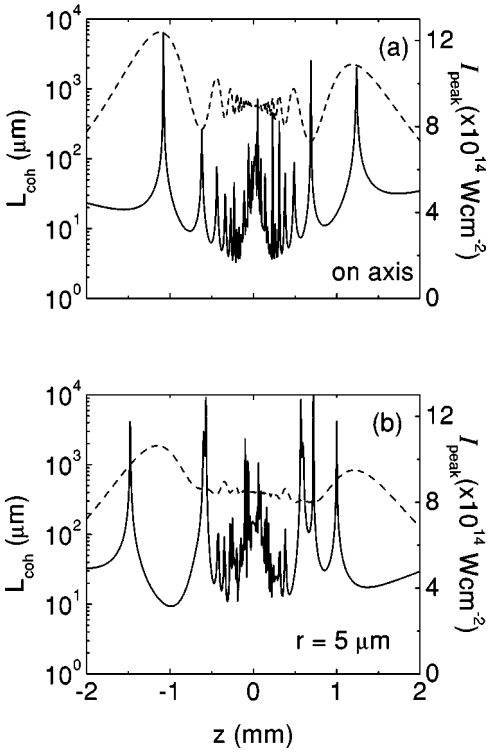

FIG. 8. Coherence length vs z (solid line) for the 45th harmonic in neon, on-axis (a) and at $r=5$ μm (b). The dashed lines in both plots represent the laser peak intensity, expressed in units of 10^{14} W cm^{-2}.

phase behavior and its variation cannot be compensated by that of Φ_{TB}. The good phase-matching region is now restricted to the much smaller area 1.1 mm$<z<$1.3 mm.

The z dependence of L_{coh} is shown in Fig. 8 (solid line) for H45, and a laser intensity of 9×10^{14} W cm^{-2}, on-axis [$z=0$, case (a)], and for $r=5$ μm [case (b)]. The dashed line is the local laser intensity $I(r,z)$. Several isolated spikes of high coherence length appear in both cases. The main feature is that the high coherence spikes (divergences) tend to accumulate around $z=0$, where, although with lower amplitudes, they form an extended region of good phase-matching conditions, thus allowing the growth of the macroscopic harmonic field. Similar behavior is also obtained for other harmonics.

It is interesting noticing that while the correlation between coherence length spikes and maxima and minima of the laser intensity is strict on-axis, it gets much poorer off-axis. This is because $\nabla\Phi_{TB}(r,z)$ in Eq. (7) has a negligible z component in both cases, but its radial component vanishes on-axis, where $\Phi_{TB}(r,z=\text{const})$ shows a hump, whereas it does not at $r=5$ μm. Hence, for $r=0$ only the atomic dipole phase determines the behavior of L_{coh}, whereas off-axis the geometric phase Φ_{TB} gives also a contribution.

Let us now discuss how the coherence map approach can be used to obtain useful information on the spatial direction of the emitted harmonic fields. First of all, we note that the coherence length map of the qth harmonic, obtained through Eq. (5), is based only on the amplitudes of the vector fields $\boldsymbol{k}_{pol}$ and $\delta\boldsymbol{k}_{disp}$ (see the Appendix). Thus, the map of L_{coh} does not contain any physical information about the direction of the emitted contributions to the qth harmonic field.

This information is instead contained in the direction of the wave vector of the nonlinear polarization field, namely $\boldsymbol{k}_{pol}$, that determines in each point of the interaction region the direction of the contribution to the qth harmonic field emitted in that point. A typical (r,z) map of the directions of $\boldsymbol{k}_{pol}$ is shown in Fig. 9 for the 45th harmonic at a laser intensity of 9×10^{14} W cm^{-2}. In the same figure we also report the contour plot of the nonlinear dipole intensity, evaluated as $\propto I^5(r,z)$, which provides the spatial weight coefficient for each elemental harmonic contribution. Two lobes of high nonlinear dipole intensity, located at $z\approx\pm1.3$ mm, are clearly visible on both sides of the focus ($z=0$). In these two regions the nonlinear dipole intensity is up to five to seven times higher than around $z=0$. We have plotted an additional column of vectors just in correspondence of the high-intensity lobe centered at $z\approx-1.3$ mm in order to evidence how a large spatial gradient of the nonlin-

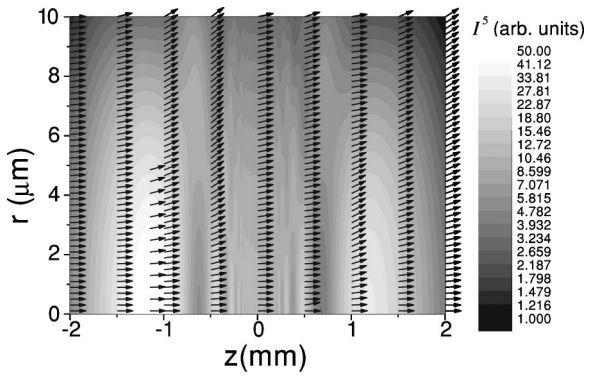

FIG. 9. Contour plot of the nonlinear dipole intensity, $\propto I^5(r,z)$, in the interaction region. White/black tones denote high/low nonlinear dipole intensity values, displayed by using a log scale. The arrows indicate the direction of the elemental contribution to the 45th harmonic field, $\delta \boldsymbol{E}_{45}$, for a laser intensity of 9×10^{14} W cm^{-2}. The harmonic divergence angle θ is reported on a linear scale, but magnified by a factor of 20, in order to evidence its variations throughout the interaction region. Actual θ values range between 0 and 40 mrad.

ear dipole moment affects the emission direction of the harmonic wavelets. Clearly, harmonic wavelets emitted from this lobe exhibit a strongly increasing divergence with increasing r value. This highlights the negative role played by strong spatial gradients of the nonlinear dipole moment from the point of view of keeping the generated harmonic beams well collimated along the z axis. Furthermore, in the regions around $z \approx \pm 1.3$ mm, phase matching is rather poor, as shown in the coherence length maps of Fig. 6. Obviously, this does not support a constructive superposition of the harmonic wavelets there generated.

Finally, we remark that the elementary contributions to the harmonic fields emitted in the two lobes at $z \approx \pm 1.3$ mm are characterized by rather large emission angles ($\simeq 10$ mrad), thus giving rise to highly divergent harmonic beams. On the contrary, the elementary contributions to the 45th harmonic emitted in a rather large region around $z = 0$, where phase-matching conditions are good [see Fig. 6(b)], show much smaller divergence angles ($\approx 2-3$ mrad]. This implies that 45th harmonic radiation generated in the focal region is more collimated and spatially coherent than that emitted by other areas of the interaction zone. For the sake of completeness, we have verified that other harmonics in the plateau show similar behavior.

V. HARMONIC DIVERGENCE ANGLES

In this section we discuss a simple method, based on the graphical approach of the coherence length map, which allows one to estimate the divergence angle θ of the harmonic beams produced in the nonlinear interaction of TB, few-optical-cycle laser pulses and gas atoms.

In the usual approach used to obtain the final harmonic field pattern produced in the gas medium, each single elementary contribution to the qth harmonic field, $\delta \boldsymbol{E}_q(r,z)$, is propagated and added to the built-up harmonic field. This obviously requires solving the harmonic field propagation equation to achieve a rigorous solution (see, e.g., Ref. [24]).

We have instead developed a simple algorithm to add up all the elementary harmonic wavelets $\delta \boldsymbol{E}_q(r,z)$. Beyond its simplicity, our method has the noticeable advantage of evidencing the physical role of the quantities involved in the process of HOH generation, and has allowed us to estimate the dependence of harmonic beam intensity I_q on the far-field divergence angle θ. Although approximated, our approach has produced numerical predictions which turn out to be in very good qualitative and quantitative agreement with the features observed in the actual experiments.

Since the laser pump beam is linearly polarized, the harmonic field E_q will be linearly polarized in a direction parallel to the fundamental electric field. Our method is then based on the following two assumptions: (1) only wavelets δE_q emitted under the same divergence angle θ will interfere; (2) wavelets emitted under the same divergence angle $\delta E_q(\theta)$ interfere as they were plane waves.

The first statement is very well fulfilled in the far field, where harmonics are detected in the actual experiments. In fact, single harmonic field contributions emitted at different angles will spatially disperse in the far field.

Also the second statement represents a very good approximation in the far field, where the radius of curvature of each selected elementary contribution becomes extremely large and the plane-wave approximation holds true.

Within the above approximation, by denoting with $\delta E_{q_i}(\theta)$ the wavelet of the qth harmonic field emitted at the point (r_i, z_i), in the direction θ, the harmonic intensity $I_q(\theta)$ is given by

$$I_q(\theta) = \left| \sum_i \left[\delta E_{q_i}(\theta) \right] \right|^2 = I_q^{(dip)}(\theta) + 2 I_q^{(PM)}(\theta), \quad (8)$$

where

$$I_q^{(dip)}(\theta) = \sum_i \left| \left[\delta E_{q_i}(\theta) \right] \right|^2,$$

$$I_q^{(PM)}(\theta) = \sum_{i,j \neq i} \left[\delta E_{q_i}(\theta) \right] \left[\delta E_{q_j}(\theta) \right] \cos(\phi_i - \phi_j), \quad (9)$$

and the sum index i runs over all the points (r_i, z_i) of the gaseous medium. In Eq. (8) the far-field harmonic intensity $I_q(\theta)$ has been explicitly split into the sum of two contributions. The first contribution $I_q^{(dip)}(\theta)$ only depends on the nonlinear dipole contribution, thus reflecting the single-atom response, whereas the second one, $I_q^{(PM)}(\theta)$, depends on the relative phase $\phi_i - \phi_j$ of each couple of emitted harmonic wavelets and contains all the phase-matching effects.

The phase ϕ_i of $\delta E_{q_i}(\theta)$ in Eq. (9) is given by

$$\phi_i(r_i, z_i, \theta) = \phi_i^{(0)}(r_i, z_i) + \Delta \phi_i(z_i, \theta), \quad (10)$$

with $\phi_i^{(0)}$ and $\Delta \phi_i$ given, respectively, by [see Eq. (7)]

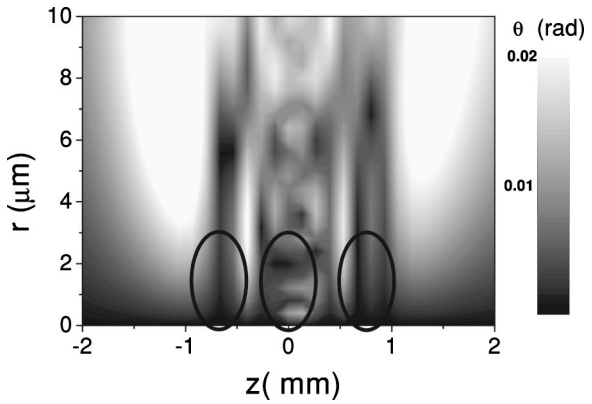

FIG. 10. Contour plot showing the 2D distribution of the elemental contribution divergence angle θ in the interaction region for the 69th harmonic in neon. The laser intensity is 9×10^{14} W cm^{-2}. The three most extended regions of lowest divergence are marked by closed lines.

$$\phi_i^{(0)}(r_i,z_i)=q\Phi_{TB}(r_i,z_i)+\Phi_{dip}(r_i,z_i),$$

$$\Delta\phi_i(z_i,\theta)=k_q\frac{\overline{z}-z_i}{\cos\theta}, \tag{11}$$

where $\phi_i^{(0)}$ is the initial phase of the harmonic wavelet emitted at the point (r_i,z_i), and $\Delta\phi_i$ accounts for the propagation from the emission point (r_i,z_i) to the far-field $(z=\overline{z})$. Once $I_q(\theta)$ has been worked out, it is possible to define an overall harmonic beam divergence angle $\overline{\theta}_q$ as the weighted average of θ with the harmonic intensity as weight coefficient:

$$\overline{\theta}_q=\frac{\int_0^{\theta_{max}}\theta I_q(\theta)d\theta}{\int_0^{\theta_{max}}I_q(\theta)d\theta}, \tag{12}$$

where $\theta_{max}=10$ mrad is the maximum angular tangential acceptance of the experimental apparatus [46].

Finally, $\overline{\theta}_q$ has been compared to the measured FWHM value of the far-field angular, harmonic intensity pattern. It is worth pointing out that typically $\overline{\theta}_q$ has been calculated by using 400 points along the z direction and 50 points along the radial direction. This implies longitudinal and radial steps, δz and δr, of 2.5 μm and 0.25 μm, respectively. We stress that the evaluation of $\overline{\theta}_q$ turns out to be rather stable and is not significantly modified when making δz and δr smaller by a factor of 4.

As a general characteristic, θ never exceeds $\approx$40 mrad, but is typically much smaller in regions where the harmonic field considerably grows up. The most extended of these regions is around $z=0$ where, depending on the laser peak intensity and on the harmonic order, θ ranges from few up to about 10 mrad. These features are illustrated in Fig. 10 where we report the local values of θ for H69 at a laser intensity of 9×10^{14} W cm^{-2}. It is clear that the harmonic wavelets are

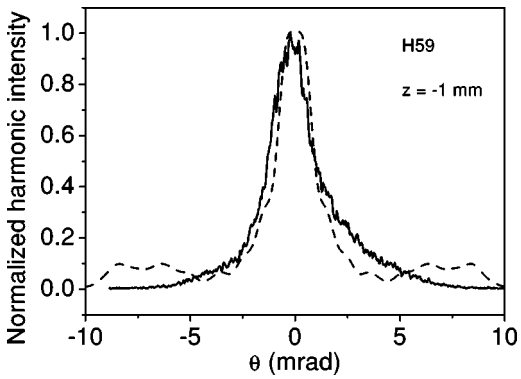

FIG. 11. Calculated (dashed line) and measured (solid line) far-field intensity patterns of the 59th harmonic generated at $z=-1$ mm as a function of the angular coordinate θ (laser intensity of 9×10^{14} W cm^{-2}).

emitted with a very low divergence angle in three large areas (marked in the figure) around $z=0$ and symmetrically located at the left and right sides of the origin, between $z\approx-1$ mm and $z\approx-0.5$ mm and $z\approx0.5$ mm and $z\approx1$ mm, respectively. The 0.5 mm$\leqslant z\leqslant$1 mm area does not efficiently contribute to the harmonic field generation because the nonlinear atomic dipole reaches rather low values there (see Fig. 9). The remaining two marked areas exhibit features that completely agree with that reported in Ref. [16]: in this paper, in fact, the lowest harmonic divergence was typically observed at $z=-1$ mm and the highest harmonic brightness in the range -1 mm$<z<0$. Other zones of the map also show a very small divergence angle, but phase matching greatly favors the region in proximity of $z=0$. The two lobes of highest laser intensity at $z\approx\pm1.3$ are characterized, mainly off-axis, by rather large values of θ.

As an example of the angular dependence of the calculated harmonic intensity pattern, in Fig. 11 we plot $I_{59}(\theta)$ for $z=-1$ mm (dashed line) together with the corresponding measured profile (solid line). The calculated curve, beyond the central narrow peak, shows an additional lower and wider ring. Such a feature agrees with the theoretical analysis performed in Ref. [16] by numerically integrating the harmonic propagation equation, but is absent in the measured profile. We note that it would be, however, very hard to experimentally observe the additional ring by means of the setup used in Ref. [16]. The profile measured in that experiment, indeed, is just a projection of the whole, cylindrically symmetric, harmonic beam onto the spatial axis of the detector.

Finally, in Figs. 12 and 13 we compare the harmonic divergence angle calculated by our model with the corresponding measured values (affected by a 15% statistical uncertainty). The figures refer to a laser intensity of 9×10^{14} W cm^{-2}. In Fig. 12 the measured and calculated divergence angle is plotted versus z for a middle-plateau harmonic [H45 in Fig. 12(a)], and for a close-to-the-cutoff harmonic [H59 in Fig. 12(b)]. The general quantitative agreement between calculated and measured divergence angles is satisfying. The prediction of our model just slightly underestimates the harmonic divergence values. The general trend of the measured divergence angles, increasing with z in

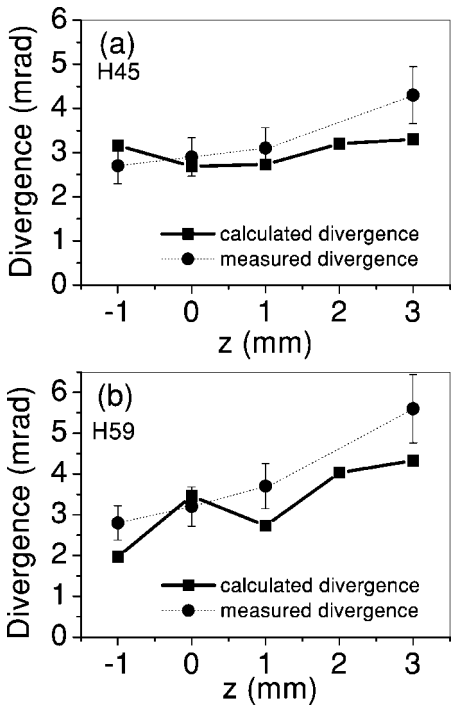

FIG. 12. Calculated (squares) and measured (circles) harmonic divergence angles vs z for H45 (a) and for H59 (b). The laser intensity is 9×10^{14} W cm^{-2}.

both (a) and (b), is well reproduced. In the case of H45 the calculated point at $z=-1$ mm overestimates the measured value, although within the error bar. In Fig. 13 calculated and measured divergence angles are reported as a function of the harmonic order at $z=0$. Calculated and measured values agree very well within the experimental errors and the behavior of the measured values, increasing with the harmonic order, is reproduced by the simulated values. Such behavior can be interpreted in the following way: for plateau harmonics the dominant contribution to the harmonic phase, $\Phi_{tot}^{(plateau)}(r,z)$, comes from the dipole phase which is the same for all the harmonic orders within our approximation. Therefore, the harmonic beam divergence is nearly constant with the harmonic order. For cutoff harmonics, instead, as seen above [Fig. 7(b)], the dipole phase is almost twice

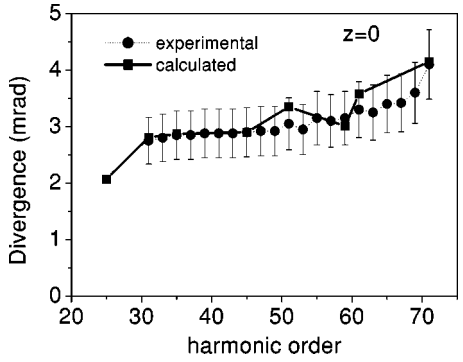

FIG. 13. Calculated (squares) and measured (circles) harmonic divergence angles vs the harmonic order for $z=0$. The laser intensity is 9×10^{14} W cm^{-2}.

smaller and the geometric phase $q\Phi_{TB}(r,z)$ is increasingly relevant. Since $q\Phi_{TB}(r,z)$ has a considerable radial gradient component just in the best phase-matching region -1 mm $<z<0$, where the macroscopic harmonic field grows up, the harmonic divergence becomes correspondingly larger with increasing harmonic order.

VI. DISCUSSION AND CONCLUSIONS

The presently increasing use of ultrashort sub-10-fs pulses, produced with the hollow fiber compression technique, to generate high-order harmonics in gases has urged us to investigate the influence of the truncated-Bessel nature of the fundamental pumping beam on the nonlinear generation process. Our analysis has also been strongly stimulated by the need of interpreting the somewhat surprising differences observed when using a TB-pump beam with respect to the case of Gaussian pump beams.

We have, thus, developed a very simple and versatile numerical model which is essentially based on the well-known problem of the phase-matching conditions for HOH generation in the interaction region, revisited in view of the different spatial mode of the TB-pumping beam intensity. Our model, which mainly rests on the assumption of a pump-laser beam which is substantially unperturbed when passing through the gas jet, evaluates the potential efficiency of each point of the laser-gas interaction region to produce an elementary contribution to the emitted harmonic field which is capable to add up constructively to the contributions originated by other points. This leads to a two-dimensional coherence length map, extended to all the nonlinear generation region. The coherence length map takes into account all the contributions to the harmonic field phase, namely, the intrinsic dipole phase and the geometric phase, both strongly dependent on the spatial mode of the pumping beam.

By starting with these coherence length maps, we have, then, discussed how one can very simply reconstruct the whole far-field wave front of the harmonic fields, thus obtaining the final spatial profiles and divergence angles of harmonics.

Our approach, although approximated, has a number of considerable advantages. First of all, it produces a sound and direct physical evidence of the role played by the different spatial intensity and phase distributions of Gaussian and TB-pump beams in HOH generation. Second, it is very simple and rapid, since all the considerable physical information that it provides is obtained by simply calculating the spatial distribution of the TB-pump beam and the single-atom response, namely, the amplitude and phase of the nonlinear dipole moment. One, thus, avoids the problem of solving the fundamental and harmonic field propagation equations and of exact calculation of the nonlinear dipole moment, which are both numerically heavy and time consuming. Finally, it can be easily generalized to other pump-laser geometries.

By using the coherence length map approach we have thus interpreted the main features observed in recent experiments carried out with few-optical-cycle TB-pumping beams, highlighting the relevant differences with the Gaussian pump beam case. We have, in particular, obtained a re-

markably good qualitative and quantitative agreement between the numerical values predicted by our model and the experimental values of the harmonic far-field spatial profiles and divergence angles, and their dependence on the harmonic order q and propagation coordinate z.

An aspect of considerable interest, which is worth stressing, is that our model fully explains the characteristic of TB-pumping beams of leading to relatively low harmonic divergence angles when the laser light is focused near the gas jet (-1 mm$\leqslant z \leqslant 0$), contrary to the case of pumping Gaussian beams. Around $z=0$ is located the largest area of the interaction region where the laser intensity is high. This leads to a conversion efficiency correspondingly high, and to the very high harmonic brightness observed in recent experiments.

As a concluding remark, it is worth pointing out that, according to our analysis, the considerable differences between the two cases of HOH generation with Gaussian and TB-pumping beams can essentially be ascribed to the different phase-matching mechanisms and not to the different pulse lengths characterizing present Gaussian ($\approx$100–30 fs) and compressed TB beams (sub-10-fs).

ACKNOWLEDGMENT

This work was partially supported by the European Community's Human Potential program under the Contract No. CT-HPRN-2000-00133 ATTO-Network.

APPENDIX: DISPERSIVE EFFECTS

In the presence of dispersion, the polarization wave vector can be separated into two contributions $\boldsymbol{k}_{pol}=\boldsymbol{k}^0_{pol}+\delta\boldsymbol{k}_{disp}$, where $\boldsymbol{k}^0_{pol}$ is the dispersion-free wave vector [see Eqs. (6) and (7)], and $\delta\boldsymbol{k}_{disp}$ can be expressed by the sum of two terms:

$$\delta\boldsymbol{k}_{disp}=\delta\boldsymbol{k}_{disp,1}+\delta\boldsymbol{k}_{disp,2} = q\frac{2\pi}{\lambda_0}\{[n(\omega_0)-1]\hat{\boldsymbol{k}}+z\boldsymbol{\nabla}n(\omega_0)\}, \qquad \text{(A1)}$$

$\hat{\boldsymbol{k}}$ being the unit vector parallel to the propagation z axis. Thus, $\delta\boldsymbol{k}_{disp,1}$ is purely longitudinal, i.e., along the z axis, and represents the mismatch vector of a plane wave that travels through a dispersive medium. On the other hand, $\delta\boldsymbol{k}_{disp,2}$ arises from the spatial inhomogeneity of the medium refractive index and contains both longitudinal and transverse components.

As a first remark, in the experimental conditions discussed in this paper, namely, a Ne medium length of less than 1 mm and a maximum local pressure of about 30–60 mbars, it turns out that the dispersion from neutrals can be neglected. This is not the case when the process of harmonic generation takes place at very high local pressure (of the order of several hundred of millibars) and/or in long, capillary waveguides (medium lengths of the order of several tens of millimeters), e.g., the works reported in Refs. [14] and [47]. The remaining contribution to the refractive index is then due to laser-induced free electrons, and $n(\omega)\approx 1-e^2n_e(\boldsymbol{r})/2\epsilon_0 m_e\omega^2$ with ϵ_0 being the vacuum dielectric constant. In such a condition, the relative weight between $\delta\boldsymbol{k}_{disp,1}$ and $\delta\boldsymbol{k}_{disp,2}$ is readily found to be

$$\frac{(\delta\boldsymbol{k}_{disp,2})_z}{(\delta\boldsymbol{k}_{disp,1})_z}=\frac{z}{n_e}\frac{\partial n_e}{\partial z},$$

$$\frac{(\delta\boldsymbol{k}_{disp,2})_r}{(\delta\boldsymbol{k}_{disp,1})_z}=\frac{z}{n_e}\frac{\partial n_e}{\partial r}. \qquad \text{(A2)}$$

In our typical experimental conditions $(\delta\boldsymbol{k}_{disp,2})_z$ can be neglected in comparison with $(\delta\boldsymbol{k}_{disp,1})_z$ as shown in Fig. 14 where $(\delta\boldsymbol{k}_{disp,2})_z/(\delta\boldsymbol{k}_{disp,1})_z$ is reported on-axis, where the nonlinear dipole intensity is generally higher. It is seen that the z component of $\delta\boldsymbol{k}_{disp,2}$ never exceeds 20% of $|\delta\boldsymbol{k}_{disp,1}|$ in the regions of physical interest, namely, where high values of the nonlinear dipole intensity are concentrated. Furthermore, in a quite extended area around $z=0$ this ratio falls well below 2%.

As for $(\delta\boldsymbol{k}_{disp,2})_r$, it vanishes on-axis for symmetry reasons, but it increases quite rapidly off-axis, becoming larger than $(\delta\boldsymbol{k}_{disp,1})_z$. Thus, as an example, we have performed a complete numerical simulation for calculating the coherence map of H45, by including all the mismatch vectors and we have compared this map with that reported in Fig. 6(b) which is obtained when all dispersive effects are neglected. This

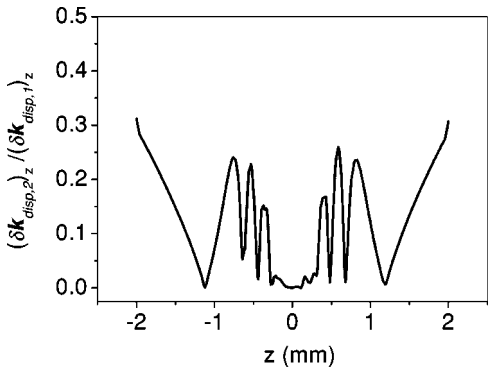

FIG. 14. On-axis ratios $(\delta\boldsymbol{k}_{disp,2})_z/(\delta\boldsymbol{k}_{disp,1})_z$ (solid line) calculated in neon for a laser peak intensity of 9×10^{14} W cm^{-2}.

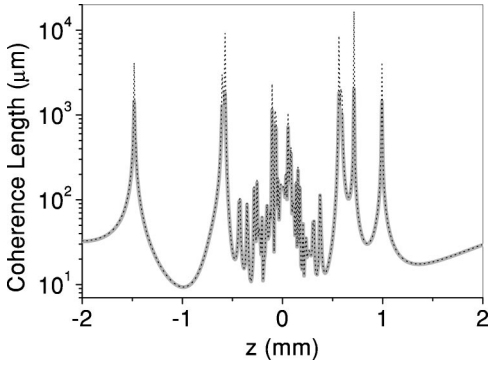

FIG. 15. Coherence length for H45 with (thick gray line) and without (dotted line) free-electron dispersion, calculated in neon for a laser peak intensity of 9×10^{14} W cm^{-2}.

comparison is reported in Fig. 15 where the broken line and the thick gray line represent the coherence length at $r=5$ μm, without and with free-electron dispersion accounted for, respectively. The only difference between the two curves is that the peak values of the coherence length, obtained when the denominator of Eq. (5) approaches zero, are considerably decreased by free-electron dispersion. Although this decrease can reach a factor of 5–10, it must be noted that its effect is limited to extremely small areas around the peaks. These areas are so small that the overall region where free-electron dispersion significantly affects the average coherence length value covers a totally negligible part of the overall harmonic generation region.

On the contrary, the average value of the coherence length within the zones where the generated harmonic field is well phase matched and effectively constructed is substantially unchanged. This feature is valid for all the investigated harmonics and for all experimental conditions of concern in this paper (e.g., a laser intensity up to 10^{15} W cm^{-2} and a gas pressure in the range 30–60 mbars).

We have also checked the influence of free-electron dispersion on the divergence angle θ of the harmonic field elemental contributions. We have, for example, found that, both for H45 (in the middle of the plateau) and H69 (in the cutoff region), the variation of θ due to the inclusion in the calculation of free-electron dispersion is typically confined to less than 0.1%.

In order to quantitatively illustrate the reasons of the negligible effect of free-electron dispersion, as an example we report in Table I the values of the components of the vectors $\boldsymbol{k}_{pol}^{0}$ and $\delta\boldsymbol{k}_{disp}$ for H45, typical of the regions ($3\,\mu\text{m}<r<6\,\mu\text{m}$), ($-1.25$ mm$<z<-0.75$ mm and 0.75 mm$<z<1.25$ mm), namely, evaluated where the free-electron density is high and its gradients reach their maximum.

TABLE I. Values of the components of the vectors $\boldsymbol{k}_{pol}^{0}$ and $\delta\boldsymbol{k}_{disp}$ evaluated at the point $z=1$ mm, $r=5$ μm. These values are typical of the regions ($3\,\mu\text{m}<r<6\,\mu\text{m}$), ($-1.25$ mm$<z<-0.75$ mm and 0.75 mm$<z<1.25$ mm), where the free-electron density gradients reach their maximum.

Vector component	Value (μm^{-1})
$(\boldsymbol{k}_q)_z=45\dfrac{2\pi n(\omega_0)}{\lambda_0}$	353.4
$\dfrac{\partial\Phi_{tot}}{\partial z}$	2.93×10^{-3}
$\dfrac{\partial\Phi_{tot}}{\partial r}$	-8.12
$(\delta\boldsymbol{k}_{disp,1})_z$	1.48×10^{-3}
$(\delta\boldsymbol{k}_{disp,2})_z$	-1.3×10^{-3}
$(\delta\boldsymbol{k}_{disp,2})_r$	2.76×10^{-1}

From the values reported in Table I it is clear that the main mismatch factor is $\partial\Phi_{tot}/\partial r$, i.e., the radial component of $\boldsymbol{k}_{pol}^{0}$, which is due to the radial gradients of Φ_{dip} and Φ_{TB}. Thus, this factor, which has been fully accounted for in our analysis [see Eq. (7)], is the only one determining both the finite value of the coherence length and the divergence angle of the elemental contributions to the macroscopic harmonic field. As a consequence, it is also the principal physical mechanism affecting the actual far-field divergence of the harmonic beams. We can, therefore, conclude that in our experiment the far-field emission angle of the harmonic field elemental contributions is not affected by free-electron dispersion, and that our assumption of neglecting such an effect is reasonably justified.

[1] T. Brabec and F. Krausz, Rev. Mod. Phys. **72**, 545 (2000).
[2] M. Drescher, M. Hentschel, R. Kienberger, M. Uiberacker, V.Y.A. Scrinzi, T. Westerwalbesloh, U. Kienberger, U. Heinzmann, and F. Krausz, Nature (London) **419**, 803 (2002).
[3] R. Haight and P. Seidler, Appl. Phys. Lett. **65**, 517 (1994).
[4] J. Larsson, E. Mével, R. Zerne, A. L'Huillier, C.-G. Wahlström, and S. Svanberg, J. Phys. B **28**, L53 (1995).
[5] M. Gisselbrecht, D. Descamps, C. Lyngå, A. L'Huillier, C.-G. Wahlström, and M. Meyer, Phys. Rev. Lett. **82**, 4607 (1999).
[6] W. Theobald, R. Hässner, C. Wülker, and R. Sauerbrey, Phys. Rev. Lett. **77**, 298 (1996).
[7] M. Schnürer, Z. Cheng, M. Hentschel, G. Tempea, P. Kalman, T. Brabec, and F. Krausz, Phys. Rev. Lett. **83**, 722 (1999).
[8] R. Haight and D. Peale, Phys. Rev. Lett. **70**, 3979 (1993).
[9] F. Quéré, S. Guizard, G. Petite, P. Martin, H. Merdji, B. Carré , and J.-F. Hergott, Phys. Rev. B **61**, 9883 (2000).
[10] F. De Filippo, C. de Lisio, P. Maddalena, G. Lerondel, T. Yao, and C. Altucci, Appl. Phys. A: Mater. Sci. Process. **A73**, 737 (2001).
[11] P. Salières, L. Le Déroff, T. Auguste, P. Monot, P. d'Oliveira, D. Campo, J.-F. Hergott, H. Merdji, and B. Carré, Phys. Rev. Lett. **83**, 5483 (1999).
[12] D. Descamps, J.-F. Hergott, H. Merdji, P. Salières, C. Lyngå, J. Norin, M. Bellini, T. Hänsch, A. L'Huillier, and C.-G. Wahlström, Opt. Lett. **25**, 135 (2000).
[13] M. Drescher, M. Hentschel, R. Kienberger, G. Tempea, C. Spielmann, G. Reider, P. Corkum, and F. Krausz, Science **291**, 1923 (2001).
[14] M. Hentschel, R. Kienberger, C. Spielmann, G. Reider, N. Milosevic, T. Brabec, P. Corkum, U. Heinzmann, M. Drescher, and F. Krausz, Nature (London) **414**, 509 (2001).
[15] P. Villoresi *et al.*, Phys. Rev. Lett. **83**, 2494 (2000).
[16] M. Nisoli *et al.*, Phys. Rev. Lett. **88**, 033902 (2002).
[17] M. Nisoli, S.D. Silvestri, and O. Svelto, Appl. Phys. Lett. **68**, 2793 (1996).
[18] C. Spielmann, N. Burnett, S. Sartania, R. Koppitsch, M. Schnürer, C. Kan, M. Lenzner, P. Wobrauschek, and F. Krausz, Science **278**, 661 (1997).
[19] M. Nisoli, S. Stagira, S. De Silvestri, O. Svelto, S. Sartania, Z. Cheng, G. Tempea, C. Spielmann, and F. Krausz, IEEE J. Sel. Top. Quantum Electron. **4**, 414 (1998).
[20] M. Nisoli, S. Stagira, S. De Silvestri, O. Svelto, S. Sartania, Z. Cheng, M. Lenzner, C. Spielmann, and F. Krausz, Appl. Phys.

B: Lasers Opt. **B65**, 189 (1997).
[21] I. Christov, M. Murnane, and H. Kapteyn, Phys. Rev. Lett. **78**, 1251 (1997).
[22] P. Salières, A. L'Huillier, P. Antoine, and M. Lewenstein, Phys. Rev. Lett. **81**, 5544 (1998).
[23] G. Tempea, M. Geissler, and T. Brabec, J. Opt. Soc. Am. B **16**, 669 (1999).
[24] E. Priori *et al.*, Phys. Rev. A **61**, 063801 (2000).
[25] M. Schnürer, Z. Cheng, S. Sartania, M. Hentschel, G. Tempea, T. Brabec, and F. Krausz, Appl. Phys. B: Lasers Opt. **67**, 263 (1998).
[26] C. Durfee III, A. Rundquist, S. Backus, C. Herne, M. Murnane, and H. Kapteyn, Phys. Rev. Lett. **83**, 2187 (1999).
[27] H. Lange, A. Chiron, J.-F. Ripoche, A. Mysyrowicz, P. Breger, and P. Agostini, Phys. Rev. Lett. **81**, 1611 (1998).
[28] M. Lewenstein, P. Balcou, M.Y. Ivanov, A. L'Huillier, and P.B. Corkum, Phys. Rev. A **49**, 2117 (1994).
[29] P. Salières, A. L'Huillier, and M. Lewenstein, Phys. Rev. Lett. **74**, 3776 (1995).
[30] Ph. Balcou, P. Salières, A. L'Huillier, and M. Lewenstein, Phys. Rev. A **55**, 3204 (1997).
[31] I. Christov, J. Zhou, J. Peatross, A. Rundquist, M. Murnane, and H. Kapteyn, Phys. Rev. Lett. **77**, 1743 (1996).
[32] Z. Chang, A. Rundquist, H. Wang, M. Murnane, and H. Kapteyn, Phys. Rev. Lett. **79**, 2967 (1997).
[33] V. Tosa, E. Takahashi, Y. Nabekawa, and K. Midorikawa, Phys. Rev. A (to be published).
[34] M. Nisoli *et al.*, Appl. Phys. B: Lasers Opt. **B74**, s11 (2002).
[35] C. Altucci, R. Bruzzese, D. D'Antuoni, C. de Lisio, and S. Solimeno, J. Opt. Soc. Am. B **17**, 34 (2000).
[36] S.A.J. Collins, J. Opt. Soc. Am. A **60**, 1168 (1970).
[37] A. Yariv, *Quantum Electronics* (Wiley, New York, 1989).
[38] A. Yariv, Opt. Lett. **19**, 1607 (1994).
[39] C. Altucci, C. Beneduce, R. Bruzzese, C. de Lisio, G. Sorrentino, T. Starczewski, and F. Vigilante, J. Phys. D **29**, 68 (1996).
[40] L. Le Déroff, P. Salières, and B. Carré, Phys. Rev. A **61**, 043802 (2000).
[41] M. Ammosov, N. Delone, and V. Krainov, Sov. Phys. JETP **64**, 1191 (1986).
[42] D. Bauer and P. Mulser, Phys. Rev. A **59**, 569 (1999).
[43] Ph. Balcou and A. L'Huillier, Phys. Rev. A **47**, 1447 (1993).
[44] J. Zhou, J. Peatross, M. Murnane, H. Kapteyn, and I. Christov, Phys. Rev. Lett. **76**, 752 (1996).
[45] L. Roos, E. Constant, E. Mével, P. Balcou, D. Descamps, M. Gaarde, A. Valette, R. Haroutunian, and A. L'Huillier, Phys. Rev. A **60**, 5010 (1999).
[46] L. Poletto, G. Tondello, and P. Villoresi, Rev. Sci. Instrum. **72**, 2868 (2001).
[47] A. Rundquist, C. Durfee III, Z. Cheng, C. Herne, S. Backus, M. Murnane, and H. Kapteyn, Science **280**, 1412 (1998).